

Tuning Porosity and Surface Area in Mesoporous Silicon for Application in Li-Ion Battery Electrodes

John B. Cook,[†] Hyung-Seok Kim,[‡] Terri C. Lin,[†] Shauna Robbennolt,[†] Eric Detsi,^{†,¶} Bruce S. Dunn,^{‡,§} and Sarah H. Tolbert^{*,†,‡,§}

[†]Department of Chemistry and Biochemistry, University of California, Los Angeles, Los Angeles, California 90095-1569, United States

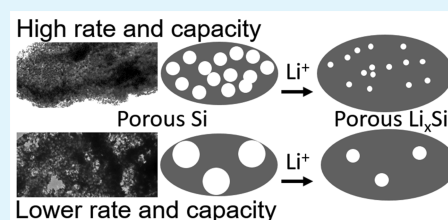
[‡]Department of Materials Science and Engineering, University of California, Los Angeles, Los Angeles, California 90095-1595, United States

[§]The California NanoSystems Institute, University of California, Los Angeles, Los Angeles, California 90095, United States

Supporting Information

ABSTRACT: This work aims to improve the poor cycle lifetime of silicon-based anodes for Li-ion batteries by tuning microstructural parameters such as pore size, pore volume, and specific surface area in chemically synthesized mesoporous silicon. Here we have specifically produced two different mesoporous silicon samples from the magnesiothermic reduction of ordered mesoporous silica in either argon or forming gas. In situ X-ray diffraction studies indicate that samples made in Ar proceed through a Mg_2Si intermediate, and this results in samples with larger pores (diameter ≈ 90 nm), modest total porosity (34%), and modest specific surface area ($50 \text{ m}^2 \text{ g}^{-1}$). Reduction in forming gas, by contrast, results in direct conversion of silica to silicon, and this produces samples with smaller pores (diameter ≈ 40 nm), higher porosity (41%), and a larger specific surface area ($70 \text{ m}^2 \text{ g}^{-1}$). The material with smaller pores outperforms the one with larger pores, delivering a capacity of 1121 mAh g^{-1} at 10 A g^{-1} and retains 1292 mAh g^{-1} at 5 A g^{-1} after 500 cycles. For comparison, the sample with larger pores delivers a capacity of 731 mAh g^{-1} at 10 A g^{-1} and retains 845 mAh g^{-1} at 5 A g^{-1} after 500 cycles. The dependence of capacity retention and charge storage kinetics on the nanoscale architecture clearly suggests that these microstructural parameters significantly impact the performance of mesoporous alloy type anodes. Our work is therefore expected to contribute to the design and synthesis of optimal mesoporous architectures for advanced Li-ion battery anodes.

KEYWORDS: silicon, high power density, high energy density, mesoporous, magnesiothermic reduction, anode, Li ion battery



INTRODUCTION

The successful widespread deployment of battery electric-drive automobiles into the marketplace relies strongly on the advent of new energy-storage materials with high energy and high power density.^{1,2} Graphite has been the negative electrode of choice for Li-ion batteries since the invention of the rocking chair technology in the early 1990s.^{3–5} However, the capacity of graphite is limited to 375 mAh g^{-1} (750 mAh l^{-1}), which is insufficient for high-energy-density applications.^{6,7} In contrast, materials that undergo alloying reactions, rather than intercalation reactions, can store significantly more charge in terms of both gravimetric and volumetric normalizations.⁸ Such high levels of charge storage result from the formation of stable high lithium content alloy phases. Silicon emerges as an attractive candidate from the collection of materials that undergo electrochemical alloying reactions with lithium, owing to its high theoretical capacity of 3579 mAh g^{-1} (2190 mAh l^{-1}), its high natural abundance, and its environmental friendliness.^{7,9}

The development of practical silicon anodes, however, has been limited because the high Li-storage capacity of silicon is associated with large ($>300\%$) volume changes, which leads to

cracking and pulverization of the active silicon material.^{10–13} As a result, more solid electrolyte interphase (SEI) forms on those freshly exposed silicon surfaces, which leads to electronic isolation and premature electrode failure. In practice, silicon base electrodes are made by mixing silicon powder with conductive additives and polymeric binders. The above-mentioned volume changes in silicon result in mechanical failure of these composite electrode structures and degradation of electronic junctions between different electrode components (silicon, conductive additive, and current collector). These degradation mechanisms ultimately lead to unacceptably short battery lifetimes for silicon-based electrodes.⁹

Nanostructuring has been shown to alleviate some of the detrimental issues related to volume changes in alloy-type materials.^{14–33} Cui and co-workers have shown that silicon nanowires accommodate volume changes extremely well, leading to improved cycle lifetimes.^{34–37} The nanoscale size and anisotropic structure reduce the interfacial strain between

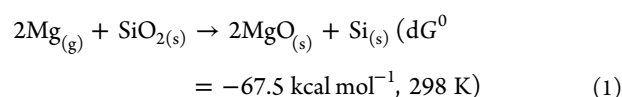
Received: December 21, 2016

Accepted: May 9, 2017

Published: May 9, 2017

the low-density lithiated phases and the higher-density nonlithiated phases during cycling. Silicon nanotubes³⁸ and hollow silicon spheres³⁹ introduce another mode to accommodate volume expansions through internal porosity. The tubular structure effectively allows the lithiated silicon to expand into the void space without pulverizing. Porous silicon nanoscale architectures have also been shown to be a promising architecture to increase the cycle lifetimes of silicon.^{40–52} One main advantage of porous nanostructures over the nanowire and nanotube nanostructures discussed above is the interconnectivity of the pore walls. This interconnectivity minimizes the problematic electronically insulating SiO₂ surface layers that would normally form at nanowire–nanowire or nanotube–nanotube junctions, which can significantly increase the overall electronic resistance of the electrode. In terms of cycling stability, the pore void space and internal surface area should lead to structures that can flex and breathe without significant cracking, leading to materials with high reversibility and longer lifetimes. In addition to the silicon nanostructures discussed above, a wide variety of nanostructured silicon materials have also been reported and reviewed.^{9,41,53–58}

Several methods exist to synthesize porous silicon with various nanoscale architectures. One effective technique that offers good control over nanoscale architecture is the magnesiothermic reduction of silica. This chemistry is similar to carbothermic reduction of silica, which requires temperatures above 1400 °C.⁵⁹ The advantage of using magnesium to reduce silica is that the reduction occurs at a much lower temperature (680 °C) compared to carbon, which enables the formation of small nanoscale structures that would otherwise coarsen at the temperatures used for carbothermal reduction.^{14,43,44,60,61} Sandhage and co-workers demonstrated that the porous structure in silica-based diatoms could be preserved using this reduction method.⁶⁰ The overall reaction is shown in eq 1;⁴⁵ the MgO product and any remaining unreacted SiO₂ are ultimately etched away with diluted HCl and HF, respectively.



This magnesiothermic reduction reaction can be used to convert various porous SiO₂ precursors into porous silicon replicas. A large library of ordered porous materials has been synthesized by sol–gel self-assembly chemistry using cationic, anionic, and nonionic structure-directing agents.^{62–67} These low-molecular-weight polymers tend to form porous silica nanostructures that can undergo significant structural coarsening even at the modest temperatures required for the chemical conversion to silicon. In response to a desire for larger porous SiO₂ structures, a number of research groups extended this templating chemistry using large block copolymers as structure-directing agents, leading to materials with pore sizes in the range of 10–50 nm.^{64,68–85} This general method has been used to synthesize mesoporous metal oxides^{69–72,77–79,81,82,84} and silica,^{64,73–76,80,85,86} with the latter being particularly relevant to this study.

Various porous silica architectures have been investigated as precursors to porous silicon using the magnesiothermic reduction method. Commercially available porous (~10 nm) SiO₂ has been converted using magnesiothermic reduction, but this small nanoscale architecture undergoes significant coarsening, with the pores growing from ~10 nm up to ~250 nm during the magnesium reduction.⁴³ Yang and co-workers

showed that a similarly nanostructured SiO₂, templated SBA-15, could be reduced to porous silicon with some retention of the original structure.⁴⁴ The synthesis conditions were similar for the two studies, except the latter report did not use hydrofluoric acid to etch residual silica from the final silicon structure. Instead, to achieve reasonable cycling stability, the sample was coated with carbon using a high-temperature process; otherwise, the capacity decay was severe.⁴⁴ Building from that work, other groups have shown that naturally derived SiO₂ with larger porous architectures, such as rice husks, can also be reduced to porous silicon and cycled effectively as a Li-ion battery anode without conductive carbon coatings.^{23,61,87}

Larger-pore porous silica can be converted to porous silicon without restructuring more easily than smaller-pore materials, but as explained above, naturally derived precursors provide little control over the starting architecture. A solution lies in the work of Richman and co-workers, who reported on the synthesis of 10–15 nm ordered porous silicon thin films from the magnesiothermic conversion of large-pore mesoporous silica.⁷⁴ While this thin-film system is extremely advantageous for fundamental studies, it is limited to low mass loading electrodes, and is not a practical energy-storage system. The methods of that study demonstrate a clear synthetic protocol for producing large-pore diblock copolymer templated silicon, which can ultimately be incorporated into traditional composite electrodes.

In this study, we have thus synthesized mesoporous silica precursor powders using large poly(butadiene-*b*-ethylene oxide) block copolymer templates as the structure-directing agent. The silica pore structure is roughly cubic and shows 3-dimensionally interconnected porosity with a cage-and-neck type structure. To better understand how variations in the silicon morphology affect the electrochemistry, the porous silica precursors are reduced to Si in two different gas environments, leading to different nanoscale structures. In situ X-ray diffraction is used to understand how those different environments lead to different pore structures. The control of morphology, through both the precisely controlled silica precursor and the reduction environment, enables the electrochemistry to be understood in terms of important structural parameters such as pore size, porosity, and surface area. While the electrode formulation has not been fully optimized in this work, we have found that the porous silicon under investigation performs quite well as a Li-ion battery negative electrode, delivering both high power and energy density along with long cycle lifetime.

■ EXPERIMENTAL DETAILS

Materials Synthesis. All starting materials were obtained from commercial suppliers and used without further purification: poly-(butadiene-*b*-ethylene oxide) $M_n = 13\,000$ (Bd/EO = 5.5:7.5), PDI = 1.04, (polymer source), tetraethyl orthosilicate (reagent grade, 98%, Sigma-Aldrich), and magnesium (–325 mesh, 99.8% metals basis, Alfa Aesar).

In a typical synthesis, mesoporous silica was synthesized by dissolving 500 mg of poly(butadiene-*b*-ethylene oxide) in 36.25 mL of ethanol at 50 °C in a closed vial. To this solution 5 mL of tetraethyl orthosilicate was added, followed by 2.5 mL of water, and finally 2.5 mL of a 1 N ethanolic solution of HCl. This solution was stirred for 20 min, and then the solution was cast into a 10-cm-diameter Petri dish and allowed to evaporate at ambient conditions. The dried sample (~1 g) was ground well in a mortar and pestle, dispersed in 12 mL of H₂O, and hydrothermally treated in a 25 mL autoclave at 130 °C for 24 h. The resulting product was washed with water three times and dried at

100 °C. This powder was calcined under flowing O₂ at 450 °C for 16 h to yield a light yellow to white powder.

In a typical synthesis, mesoporous silicon was synthesized from the solid-state reaction of magnesium and mesoporous silica. Typically, 300 mg of mesoporous silica was ground in an agate mortar with 300 mg of magnesium with a small amount of ethanol. The mixture was reacted in a graphite boat with a loosely fitted stainless steel lid. The reaction mixture was ramped to 680 °C at 11° min⁻¹ and held at this temperature for 3 h in either flowing argon or forming gas (95% N₂/5% H₂). The resulting powders (~250 mg) were soaked in 30 mL of a 0.5 N HCl ethanol solution (appropriate amount of 12.1 M HCl dissolved in 200-proof ethanol) for 2 h while being vigorously shaken. The solution was decanted, replaced with 0.5 N HCl ethanol solution, and allowed to soak again for 2 h. Finally, to ensure all the MgO was removed, the solution was decanted once more, replaced with another 30 mL of aqueous 1 M HCl, and allowed to soak for another 2 h. The HCl solution was decanted and replaced with 10 mL of an aqueous 5% HF solution, which was then soaked without agitation for 30 min. (*The addition of the HF solution must be done slowly. The reaction of HF and SiO₂ can cause the solution to splash out of the container.*) The porous silicon was washed with 500 to 1000 mL of water using vacuum filtration until the pH of the eluent was ~7. The powder was finally dried overnight in vacuum at 70 °C.

Materials Characterization. Powder X-ray diffraction (XRD) was performed in a PANalytical X'Pert Pro operating with Cu K α ($\lambda = 1.5418$ Å) using a 0.03° step size, a voltage of 45 kV, and a current of 40 mA. XRD patterns were recorded in the range of 10° < 2 θ < 80°. The in situ X-ray diffraction heating study was also performed in a PANalytical X'Pert Pro, using an Anton Paar HTK 1300N high-temperature oven chamber. The heating rate was set to ~10–15°/min. A custom vacuum/gas flow system was used to facilitate the exclusion of air during the heating study. Transmission electron microscopy (TEM) was performed using a FEI Technai T12 operating at 120 kV. Nitrogen porosimetry was carried out using a Micromeritics TriStar II 3020. The surface area was calculated from the adsorption branch of the isotherm between 0.04 and 0.30 P/P_0 using the Brunauer–Emmett–Teller (BET) model. The pore diameter and pore volume were also calculated from the adsorption branch of the isotherm using the Barret–Joyner–Halenda (BJH) model. The percent porosity of the materials was calculated using the pore volume and the density of bulk silicon (2.33 g cm⁻³). The micropore surface area was calculated using the Halenda thickness equation available in the Micromeritics software package. X-ray photoelectron spectroscopy (XPS) analysis was performed using a Kratos Axis Ultra DLD with a monochromatic Al (K α) radiation source. The charge neutralizer filament was used to control charging of the sample, 20 eV pass energy was used with a 0.1 eV step size, and scans were calibrated using the C 1s peak shifted to 284.8 eV. The integrated area of the peaks was found using the CasaXPS software, and atomic ratios were also found using this software. The atomic sensitivity factors used were from the Kratos library within the Casa software.

Electrochemical Measurements. Slurries were prepared according to previously published protocols and consisted of 60 wt % porous Si powder (either Ar–Si or Fg–Si powder) used as the active component for Li storage, 20 wt % vapor grown carbon fibers (Sigma-Aldrich) used as the conductive additive, and 20 wt % carboxymethyl cellulose ($M_w = 250$ K, Sigma-Aldrich) used as binder.^{88,89} The active material loading (60 wt %) used here is consistent with previous reports on nanostructured silicon-based electrodes, and we chose to use these ratios so that this work could be compared to other nanostructured silicon electrodes.^{61,87} The three components were mixed together with water by ball-milling in order to obtain a homogeneous thick paste. The slurry was then cast onto 9 μ m copper foil (MTI Corp), dried at ambient temperature for 1 h, and further dried at 70 °C under vacuum overnight to evaporate the excess solvent. The mass loading of the electrode was ~0.5 mg/cm² of active material, which is also consistent with previous reports on nanostructured silicon-based electrodes.^{48,61,87} These electrodes were assembled into home-built Swagelok electrochemical cells using lithium metal as the counter electrode, 350 μ m borosilicate glass

fiber separators (Advantec GF75, 300 nm pore size), and an electrolyte composed of 1 M LiPF₆ in a 1:1 ethylene carbonate/dimethylcarbonate solvent (Sigma-Aldrich) with 5% (v/v) added fluorinated ethylene carbonate (TCI America). Half-cell cycling was carried out on a VSP potentiostat/galvanostat (Bio-Logic) using a 1C rate that corresponds to 2000 mA g⁻¹. One galvanostatic cycle at 0.1 A g⁻¹ was used to form a stable SEI layer before performing the cycle lifetime tests at 5 A g⁻¹.

RESULTS DISCUSSION

Structural Characterization. Porous silicon was synthesized by the magnesiothermic reduction⁶⁰ of precisely designed ordered mesoporous silica powders. The mesoporous silica precursor was prepared by evaporation-induced self-assembly of tetraethyl orthosilicate (TEOS) and poly(ethylene oxide)-*block*-polybutadiene. The sol–gel chemistry of alkoxy silicon derivatives (e.g., TEOS) is well-known and involves the hydrolysis of TEOS followed by polycondensation to form silicon oxygen bonds in a network structure.⁹⁰ During evaporation, these condensates weakly associate with the block copolymer micelles to form periodic organic–inorganic structures that can then be calcined to remove the organic polymer, leaving behind an amorphous porous silica powder.^{64,73–76,80,85,86}

The mesoporous silica powder was characterized by scanning electron microscopy (SEM), small-angle X-ray scattering (SAXS), and nitrogen porosimetry (Figure 1). The SEM in Figure 1a shows the micrometer-sized grains of the silica powder, while higher magnification of the surface of one grain in Figure 1b shows the ordered pore system. The SAXS pattern of mp-SiO₂ (mesoporous silica) is shown in Figure 1c, and the strong peak at 0.48° ($d = 19$ nm) confirms the long-range periodicity of the porous architecture. Some higher-order peaks

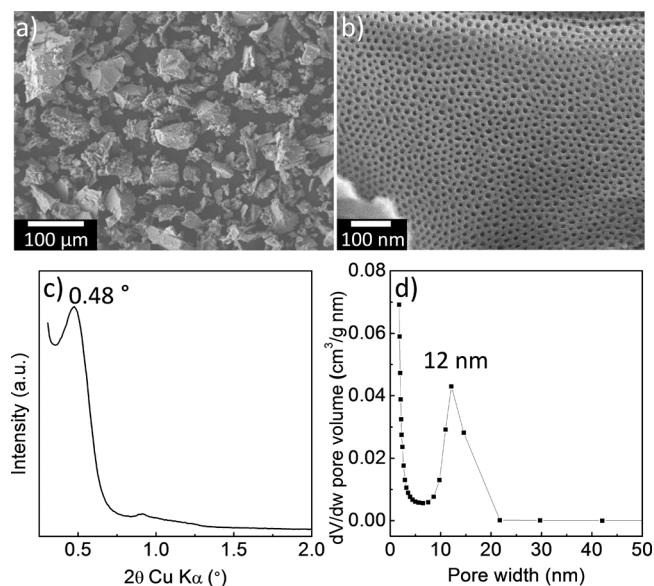


Figure 1. Scanning electron microscopy (SEM) images of mesoporous silica synthesized through a sol–gel-based, diblock copolymer templating method (a, b). The porous powder is composed of 1–100 μ m grains consisting of ordered pores. The low angle scattering of mp-SiO₂ shows one main peak at 0.48°, which corresponds to a d -spacing of 19 nm (c). Weaker higher-order peaks are also observed. Barret–Joyner–Halenda pore size distribution of mp-SiO₂ calculated from the nitrogen adsorption isotherm gives a pore width of 12 nm, in excellent agreement with the SEM images (d).

can also be seen, but they are not well enough resolved to index to a cubic pore system. Nitrogen adsorption was also carried out to measure the surface area and pore size distribution. Nitrogen adsorption isotherms shows an IUPAC convention type-IV curve (Figure S1) with sharp capillary condensation at a relative pressure ca. $0.8 P/P_0$, indicating a narrow pore size distribution. The average pore diameter was calculated as 12 nm from modeling the adsorption isotherm using the Barret–Joyner–Halenda (BJH) analysis (Figure 1d).⁹¹ This mesoporous silica has a total surface area of $356 \text{ m}^2 \text{ g}^{-1}$, a micropore surface area of $240 \text{ m}^2 \text{ g}^{-1}$, and a pore volume of $0.23 \text{ cm}^3/\text{g}$, which is consistent with previous reports utilizing similar sized polymers.⁸⁶ These micropores were produced from thermal degradation of the poly(ethylene oxide) portion of the block copolymer that was embedded in the solid silica walls. Such high surface areas are not particularly desirable for Li-ion battery anodes, but much of the surface area derived from these micropores will coarsen upon conversion to silicon, making these silica powders ideal architectures to convert to mesoporous silicon.

The mesoporous silica powder templates were converted into porous silicon using magnesium as a reducing agent in two different gas environments. The porous silicon material was reduced in either argon (Ar–Si) or a 5% hydrogen balanced with nitrogen mixture (Fg–Si) following the reaction scheme in eq 1. As a result of the large thermodynamic driving force for formation of MgO, silicon and MgO are generated from the reaction between silica and magnesium. The XRD of the reaction products before acid etching is shown in Figure 2a and b. The predominant crystalline phases are silicon (JCPDS card no. 27-1402) and MgO (JCPDS card no. 45-0946). The MgO

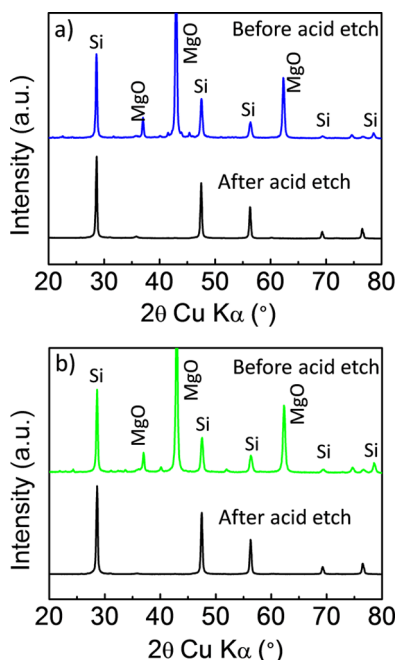


Figure 2. X-ray diffraction of Ar–Si (a) and Fg–Si (b) before acid etching and after etching in HCl and HF. Several crystalline phases (Si, MgO, and Mg_2Si) are present in the samples as a result of the reduction reaction of mp-SiO₂ with Mg. The more chemically active magnesium-containing phases are etched into aqueous species with dilute HCl. Finally HF is used to etch away any silica that remains. After this chemical etching process, both samples are pure-phase silicon.

is removed from the structure using dilute HCl, leaving pure-phase silicon. The average crystallite sizes of Fg–Si and Ar–Si after acid etching, calculated from the Scherrer equation, are 35 ± 1 and 39 ± 2 nm, respectively. These crystallite sizes are effectively the same, which indicates that the crystallographic nature of the two samples is nearly identical. The implication of this result is that any crystallographic influences on the cycling performance is the same for each sample, which allows clear relationships to be understood between structure (porosity, pore size, and surface area) and electrochemistry.

The electron microscopy images in Figure 3 show the unique pore structure afforded by the reduction of the porous silica templates. The low-magnification TEM images of the micrometer-sized grains illustrate that these particles are homogeneously porous. Further analysis of the surface of these grains using SEM shows that the nanoscale architecture consists of roughly spherical pores and randomly shaped pore walls. The TEM images in Figure 3c and f show that the wall sizes in both samples are <50 nm. This unique porous structure in both samples affords ample void space for volume change, while the nanosized pore walls enable fast charge storage through short ion diffusion path lengths. However, it is difficult to concretely distinguish the structural differences between the two samples using TEM and SEM alone. Therefore, we also characterized the nanoscale structure using nitrogen porosimetry, which led to a clear distinction between the two samples.

Analysis of the samples using nitrogen adsorption enabled us to clearly understand the structural differences between the two samples through quantification of the average pore size, total porosity, and surface area. Before acid etching, all silicon samples show minimal porosity or surface area, as all pores are presumably filled with MgO (Table 1). After acid etching, highly porous materials are formed with total pore volumes of 0.22 and $0.30 \text{ cm}^3/\text{g}$ for Ar–Si and Fg–Si, respectively. From the total pore volume, and the bulk density of silicon, the calculated porosities for Ar–Si and Fg–Si are 34% and 41%, respectively. Figure 4 shows the BJH pore size distributions of mp-Si, Ar–Si, and Fg–Si, which were calculated from the nitrogen isotherms shown in Figures S2 and S3. The reduction leads to an enlargement of the average pore size, compared to the parent mp-SiO₂, as was reported in previous studies.^{44,61} The average pore size of Fg–Si increases from 12 to 40 nm compared to Ar–Si, which increases to more than 90 nm (Figure 4 and Table 1). In addition, the BJH distributions in Figure 4 show some secondary porosity in both samples below 20 nm. Likely, this porosity resulted from etching MgO and SiO₂ during acid washing. The surface areas of the Fg–Si and Ar–Si samples are 70 and $50 \text{ m}^2 \text{ g}^{-1}$, respectively. This reduction in surface area compared to the mesoporous silica precursor is expected and results from thermal coarsening in which the extremely small micropores collapse. Again, those micropores accounted for a significant portion of the total surface area in mp-SiO₂ ($240 \text{ m}^2 \text{ g}^{-1}$). Reducing the surface area is in fact advantageous because high surface area alloy anodes decompose a significant amount of electrolyte through SEI formation, leading to poor performance characteristics.

The porosity and the distribution of that pore volume is also uniquely different in each sample. Figure 5 shows the cumulative pore volume of each sample; the total pore volume between 50 and 175 nm is basically the same for each sample. However, the Fg–Si samples show twice the specific pore volume below 50 nm compared to the Ar–Si sample. As a result, the porosity and surface area are both larger for Fg–Si

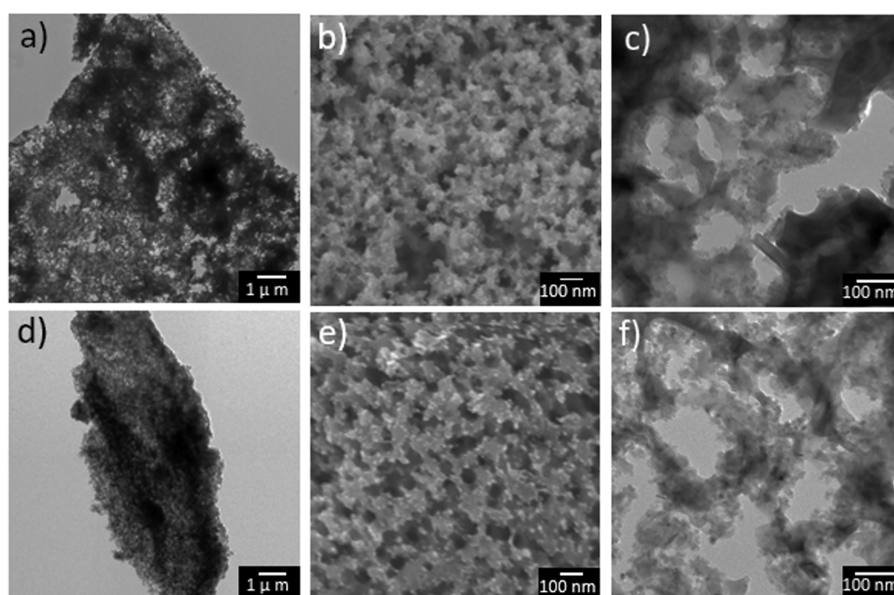


Figure 3. TEM and SEM images of Ar-Si (a, b, c) and Fg-Si (d, e, f). The low-magnification TEM images (a, d) show that the micrometer-sized particles are porous throughout, and the SEM images (b, e) and high-magnification TEM images (c, f) show that the pore walls are <50 nm. The sub-50 nm walls increase the electrochemical kinetic performance and accommodate the stress associated with repeated volume changes during cycling, enabling longer cycle lifetimes.

Table 1. Structural Characterization For Porous Samples

sample name	BET surface area (m ² g ⁻¹) ^a	pore volume (cm ³ g ⁻¹) ^b	% porosity	average pore size (nm)
mp-SiO ₂	356	0.23	33	12
unetched Ar-Si	2		3	
Ar-Si	50	0.22	34	90
unetched Fg-Si	5		7	
Fg-Si	70	0.30	41	35

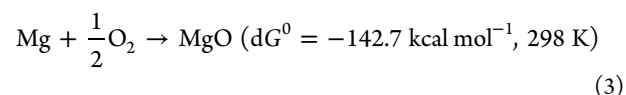
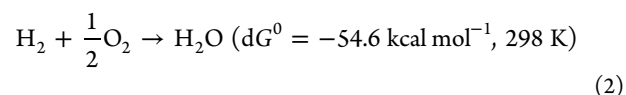
^aValues for surface area were calculated using the Brunauer–Emmett–Teller model. ^bValues for porosity and average pore size were calculated using the Barrett–Joyner–Halenda model using the nitrogen adsorption isotherms of the various samples.

(Table 1). This enables Fg-Si to perform better in several electrochemical performance categories, which will be discussed in the following **Electrochemical Measurements** section.

We have also performed high-resolution X-ray photoelectron spectroscopy (XPS) to characterize the surface chemistry and measure the extent of surface oxidation of the mesoporous silicon. Figure S4 shows the deconvoluted XPS spectra of both Fg-Si and Ar-Si. The spectra can be categorized into three regions: zerovalent silicon, silicon suboxides corresponding to Si¹⁺ (Si₂O), Si²⁺ (SiO), and Si³⁺ (Si₂O₃), and finally Si⁴⁺ (SiO₂).⁹² The binding energies in these three regions correspond well to binding energy values reported elsewhere.⁹² The zerovalent silicon signal between 98–100.5 eV can be clearly deconvoluted into two separate peaks corresponding to the P_{1/2} and P_{3/2} splitting due to J-coupling. The presence of both silicon and silicon oxides in the XPS spectra indicates that the surface of the material is only covered with a thin silicon oxide layer, which is likely reduced to Li₂O and silicon during the first electrochemical cycle.

Previous studies indicate that the highly exothermic nature of the reaction of magnesium with silica can cause an increase in local temperature to >1300 °C, which can cause severe

degradation of the fine nanostructure.⁹³ We hypothesize that the Fg-Si retains its structure better than Ar-Si because the 5% hydrogen gas present in the reducing atmosphere can react with any parasitic oxygen that is present in the reaction environment (eq 2). This scavenging reaction is far less exothermic than the oxidation of magnesium (eq 3) and so could reduce the extra heat generation, reducing further coarsening of the nanoscale architecture. In this manner, the type of gas used during the reduction can potentially drastically affect the final morphology of the reduced product, even if the gas does not directly participate in the reaction.



To further test this hypothesis, we performed in situ X-ray diffraction studies on Ar-Si and Fg-Si to gain insight into the formation mechanism of these materials, as well as to further understand how the reaction atmosphere affects the nanoscale architecture (Figure 6). When forming gas is used in the reaction environment, the reaction proceeds according to eq 1, forming Si and MgO at the expense of SiO₂ and Mg above 550 °C. The reaction products form faster than the time scale of the diffractometer scan (~5 min) and are stable during a 1 h isothermal hold at 650 °C. When argon is instead used as the reaction atmosphere, markedly different reaction products are observed. Again the reaction occurs above 550 °C, but now we observe a strong reflection for Mg₂Si, in addition to Si and MgO. This behavior seems to indicate that Si initially forms (possibly amorphous Si or very small Si domains), which further reacts to form Mg₂Si. During an isothermal hold at 575 °C, the Mg₂Si peak decreases in intensity while the Si peak increases in intensity. The presence of Mg₂Si as a reaction intermediate during the formation of Ar-Si may explain why

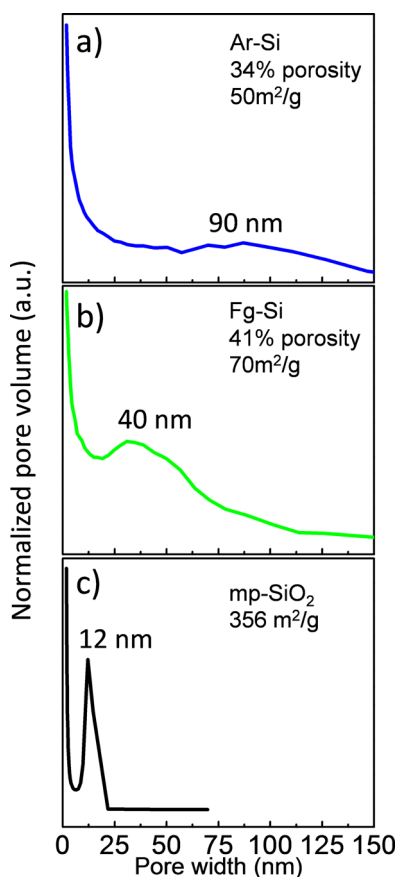


Figure 4. Comparison of Barrett–Joyner–Halenda pore size distribution for Ar–Si (a), Fg–Si (b), and mp–SiO₂ (c). This comparison shows that the Fg–Si retains the parent pore size characteristics better than the Ar–Si. The large reduction in surface area for both reduced samples is attributed to the enlargement of the pores and loss of microporosity, which are desired transformations that mitigate excessive electrolyte decomposition during electrochemical cycling.

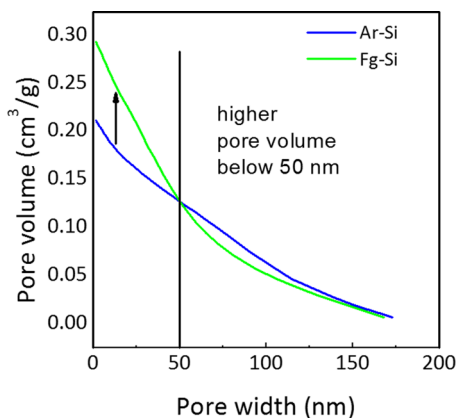


Figure 5. Cumulative pore volume vs pore width for Ar–Si (blue) and Fg–Si (green). The pore volume above 50 nm is similar for both samples, but below 50 nm Fg–Si has a significantly higher volume. This larger fraction of mesopores should be effective at accommodating volume change and facilitating fast, and reversible, charge-transfer reactions.

the nanoscale architecture is so different between the two samples and why the Fg–Si better retains the structure of the initial polymer templated silica sample. Moreover, the result

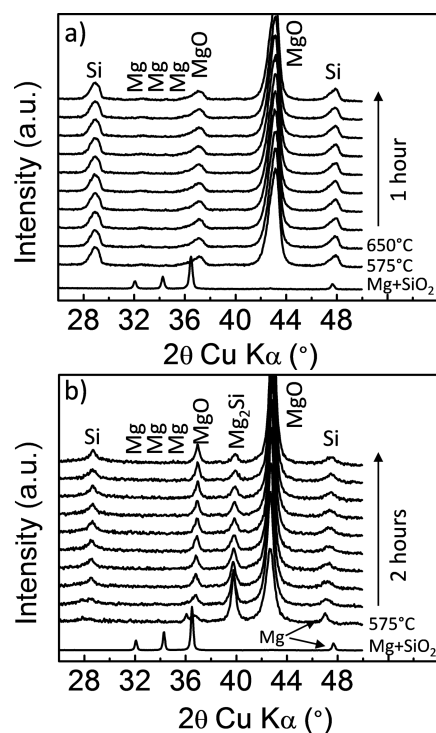


Figure 6. In situ variable-temperature X-ray diffraction of Fg–Si (a) and Ar–Si (b). Under forming gas, SiO₂ + Mg directly evolves into Si and MgO. By contrast, under pure Ar (which likely contains trace O₂), SiO₂ + Mg first evolve into MgO, Mg₂Si, and a small amount of Si. With time, the Mg₂Si signal decreases and the Si signal increases.

emphasizes the important role played by the atmosphere in these magnesiothermic reduction reactions.

Electrochemical Characterization. Silicon undergoes an electrochemical alloying reaction with lithium between 0 and 1 V (vs Li/Li⁺), storing up to 3579 mAh g⁻¹.⁹⁴ During the first lithiation process, crystalline silicon is converted to amorphous lithiated silicon between 80–120 mV, followed by the rapid crystallization of Li₁₅Si₄ below 70 mV.⁹⁴ To suppress that low potential crystallization, which could lead to premature capacity fading due to inhomogeneous volume changes between the amorphous and crystalline lithiated silicon phases, we have limited the potential range between 0.07 and 1 V vs Li/Li⁺ in this study.

The first lithium insertion process of both Fg–Si and Ar–Si at 0.1 A g⁻¹ shows redox activity between 1.25 and 0.07 V corresponding to solid electrolyte interphase (SEI) layer formation,⁹⁵ as well as formation of amorphous lithiated silicon at the expense of the pristine crystalline silicon (Figure S5).⁹⁴ During the first cycle at 0.1 A g⁻¹, the Fg–Si electrode achieves an insertion capacity of 4132 mAh g⁻¹ and a deinsertion capacity of 2947 mAh g⁻¹ while the Ar–Si achieves a lower insertion capacity of 3074 mAh g⁻¹ and a deinsertion capacity of only 2236 mAh g⁻¹, respectively. This irreversible capacity of the first cycle mainly derives from the formation of the SEI, which is thought to begin forming around 1.25 V (vs Li/Li⁺).⁹⁵ The first cycle irreversible capacity loss (ICL) values of Fg–Si and Ar–Si are 71% and 73%, respectively (Figure S5). These ICL values are similar to other high-surface-area silicon nanoparticle-based electrodes cycled with fluoroethylene carbonate (FEC) stabilizing additives.⁹⁶ More importantly, the coulombic efficiency increases to 98% by the fifth cycle for both samples, indicating that a stable SEI layer is formed during

the first few cycles and remains stable thereafter (Figure S6). The ability of both samples to form stable SEI layers is strong evidence that the porous nanoscale architecture of both samples is effective at accommodating the lithiation-induced volume changes without cracking. If the silicon active material formed cracks during this process, fresh silicon surfaces would be exposed to the electrolyte, leading to SEI growth and low coulombic efficiencies, which is not observed. The areal and volumetric capacity were also calculated from the delivered first deinsertion capacities of the individual electrodes using an electrode slurry laminate thickness of 19 μm . The areal capacities of Fg-Si and Ar-Si were 1.5 and 1.1 mAh cm^{-2} , respectively. Using the measured electrode thickness of 19 μm , the volumetric capacities of the Fg-Si and Ar-Si slurry laminates are 790 and 579 mAh cm^{-3} , respectively. While these values are reasonably high, they are not as high as they could be because the electrodes used in this work were not calendared to reduce porosity and increase density.

We now turn our attention to the kinetic performance of Fg-Si and Ar-Si. The porosity and surface area of Fg-Si are higher than those for Ar-Si (see Table 1), and as a result, Fg-Si responds with faster charge storage kinetics. Figure 7 shows the kinetic performances of Fg-Si and Ar-Si, which were galvanostatically cycled between 0.2 and 10.0 A g^{-1} . The Fg-Si electrode exhibits higher charge storage, compared to Ar-Si, at every measured rate, due to the higher surface area and higher porosity. High surface area increases the flux of Li-ions between the electrode/electrolyte interface, while the increased porosity retains open access to electrolyte during expansion. If the porosity is not large enough to accommodate the cycling-induced volume increase, electrolyte access may be cutoff to large portions of the silicon grain, leading to poorer kinetics. Comparing the actual charging and discharging time, at the fastest rate of 10 A g^{-1} , Fg-Si achieves 1121 mAh g^{-1} while Ar-Si only reaches 731 mAh g^{-1} .

In a previous study, silicon with an even smaller nanoscale structure than Fg-Si delivered 644 mAh g^{-1} at 8.8 A g^{-1} .⁶¹ This is almost 2-fold lower than the capacity of Fg-Si at 10 A g^{-1} . It is commonly thought that smaller nanoscale architectures result in faster kinetics, but these results suggest that there may be a reversal point in this trend, with very small nanostructures showing poorer performance due to increase SEI growth in very high surface area materials. Alternatively, the details of the pore's structure may play a dominant role, and that structure should be quite different in template-derived and rice-derived Si. The results of our study indicate that the nanoscale architecture of these materials forms a complicated and multidimensional optimization landscape that can be affected by pore size, wall thickness, surface area, total porosity, and details of pore architecture. Indeed the goal of our work is to provide two more defined structures to begin to understand that landscape.

Another electrochemical feature of our porous silicon electrodes is that the electrochemical reversibility of both electrodes at high current densities is extremely good. To assess the reversibility of the electrodes in this study after high rate charging and discharging, dQ/dV vs potential plots are shown in Figure S7a and b before and after the kinetic analysis. Typically, charging at high current density drives electrochemical reactions to operate far from the thermodynamic reaction potentials, making materials susceptible to deleterious kinetic processes that are not usually observed at slow rates. For example, cycling graphite at high current densities can lead to

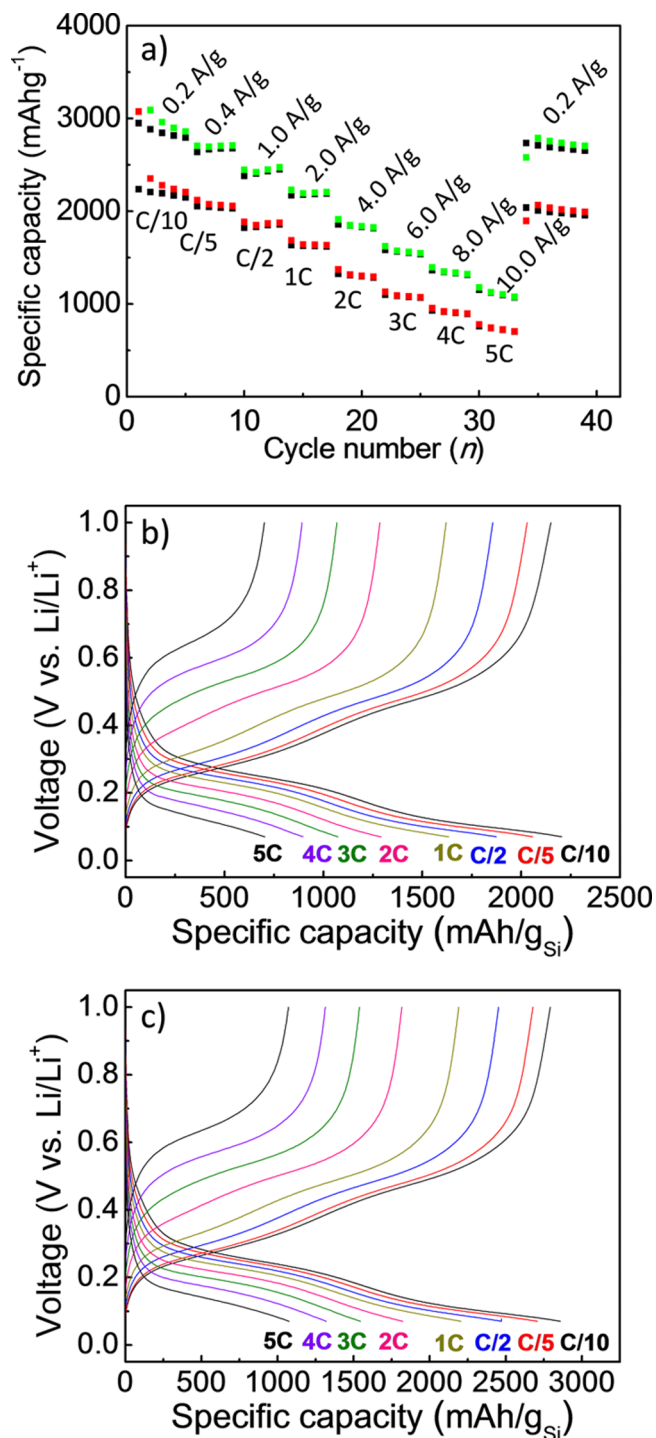


Figure 7. Kinetic performance of Fg-Si and Ar-Si between C/10–5C (a). Green and black overlapping symbols correspond to charge and discharge, respectively for Fg-Si samples, and red and black overlapping symbols correspond to charge and discharge, respectively for Ar-Si samples. Corresponding galvanostatic cycling curves for Ar-Si (b) and Fg-Si (c). Fg-Si delivers higher capacity at every rate compared to Ar-Si due to the smaller pores, higher porosity, and higher surface area.

heat generation and SEI degradation.⁹⁷ Graphite and silicon electrodes are also prone to Li-metal plating during high-rate Li-insertion, which is a serious safety concern.^{98,99} The traces in Figure S7a and b are completely superimposable indicating that

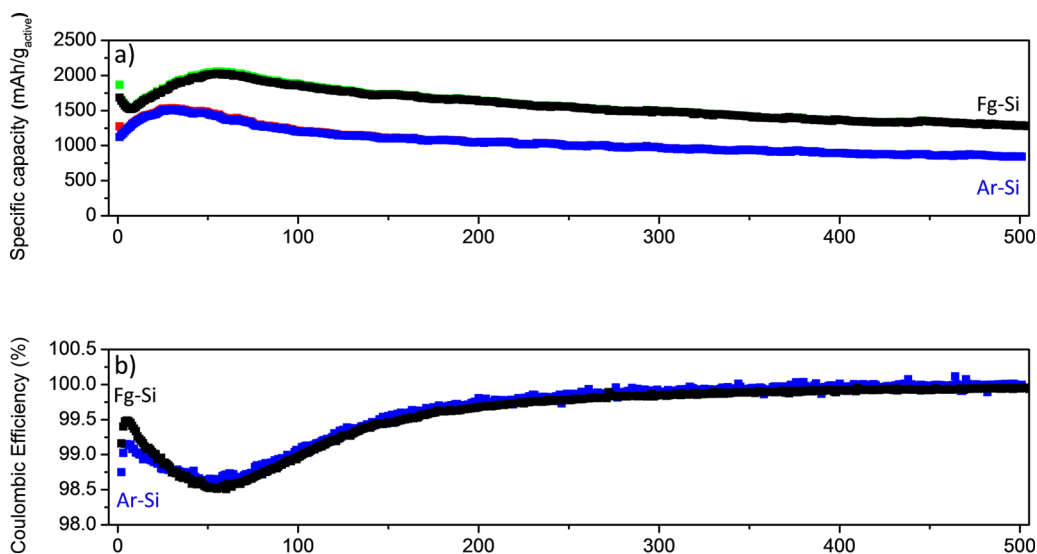


Figure 8. Cycle lifetime plots of Ar-Si and Fg-Si cycled at 5 A g^{-1} between 70 mV and 1 V vs Li/Li⁺ (a). One C/10 cycle was performed before this cycle lifetime test to form the SEI (not shown). The coulombic efficiency corresponding to the cycle lifetime plots is plotted in a separate graph for clarity (b). The long cycle lifetime and high coulombic efficiency are attributed to the porous nanoscale architecture that enables the accommodation of the volume change during cycling.

there is no change in the electrochemical processes and that no new electrochemical processes (like Li-deplating) emerge.

The excellent electrochemical reversibility of samples galvanostatically cycled at 5 A g^{-1} is shown in Figure 8a. During the first 20–50 cycles, the capacities of both samples increase slightly, and the coulombic efficiency decreases by $\sim 1\%$ over this same interval (Figure 8). The decrease does not seem to affect the long-term stability, however, and after ~ 50 cycles, the coulombic efficiency begins to increase (Figure 8b) and ultimately stabilizes at 99.95%. After 500 cycles, Fg-Si delivers 1292 mAh g^{-1} while Ar-Si only delivers 845 mAh g^{-1} . Although both samples have similar capacity retention, the increased porosity of Fg-Si probably facilitates the volume change better, enabling a higher-capacity utilization over these 500 cycles. While the composition of these electrodes has not been fully optimized for this study, the total electrode capacity (775 mAh g^{-1}) of Fg-Si after 500 cycles is still relatively high, compared to graphite, as a result of the large intrinsic capacity of silicon (Figure S8). Lower carbon and binder content could have been used in optimized electrodes to increase the total capacity even more, but the focus of this report is on studying the effects of nanoscale structure in porous silicon. Nevertheless, Fg-Si is technologically important as the capacity is nearly 1300 mAh g^{-1} after 500 charge and discharge cycles, which is still nearly 4-fold higher than the theoretical capacity of graphite, making this material system a promising candidate for the next generation of Li-ion battery anode materials.^{6,7}

CONCLUSIONS

We have demonstrated an effective approach to controlling the microstructure of mesoporous silicon. In particular, by starting with large-pore, highly homogeneous mesoporous silica materials made using block copolymer templating, and selecting an appropriate atmosphere for the reaction with magnesium, mesoporous silicon with variable pore size, porosity, and specific surface area could be synthesized. We specifically find that samples synthesized using forming gas for the magnesiothermic reduction reaction better preserve the structure of the original porous silica. High-temperature in

situ diffraction studies explain this result by showing that, under forming gas, SiO_2 and Mg evolve directly to Si and MgO, while in an argon atmosphere, an Mg_2Si intermediate is formed, which likely disrupts the nanoscale architecture of the porous solid.

The ability to control pore structure is attractive for understanding and optimizing nanoscale architecture in mesoporous silicon for application in high-performance Li-ion battery anodes. To demonstrate the impact of the nanoscale morphology of mesoporous silicon on its functional properties, we compared the electrochemical Li storage performance of mesoporous silicon with different nanoscale morphologies synthesized using different gases. Materials with smaller pore size, higher porosity, and larger specific surface area that better retained the pore structure of the initial silica material outperform the ones with larger pore size, lower porosity, and smaller specific surface area, in terms of both capacity retention (1292 vs 845 mAh g^{-1} over 500 cycles at 5 A g^{-1}) and charge storage kinetics (1121 vs 731 mAh g^{-1} at 10 A g^{-1}).

The current Si anode literature is filled with a myriad of silicon nanostructures with performances that range from excellent to poor.^{15,27,32–34,44,45} The challenge is to determine which of the many structural and electrochemical parameters are most important in determining performance when the optimization landscape is both extremely complicated and highly multidimensional. The results presented in this work shed light on the important parameters for optimizing nanoscale morphology of mesoporous silicon in a system where all variables other than nanoscale architecture are held rigorously the same. The materials themselves also show favorable performance. Perhaps more importantly, we show a route to create porous silicon from porous silica with reasonable retention of the nanoscale pore structure and a good understanding of that structure retention. It is our hope that this work will thus facilitate further optimization of next-generation Li-ion battery anode materials.

■ ASSOCIATED CONTENT

S Supporting Information

The Supporting Information is available free of charge on the ACS Publications website at DOI: 10.1021/acsami.6b16447.

Nitrogen adsorption isotherms for all samples examined in this work, XPS data for various silicon samples, and first-cycle galvanostatic traces, early-cycle coulombic efficiency plots, differential capacity plots, and total electrode capacity plots for Fg-Si and Ar-Si samples (PDF)

■ AUTHOR INFORMATION

Corresponding Author

*E-mail: tolbert@chem.ucla.edu.

ORCID 

Sarah H. Tolbert: 0000-0001-9969-1582

Notes

The authors declare no competing financial interest.

[¶]Department of Materials Science & Engineering University of Pennsylvania 3231 Walnut St., Philadelphia, PA 19104-6272, USA.

■ ACKNOWLEDGMENTS

Support for this work was provided by the U.S. Department of Energy (DOE), Office of Science, Basic Energy Sciences, under award DE-SC0014213 (S.H.T.). This funding was used principally for materials synthesis, structural characterization, and electrochemical measurements. Partial support for additional electrochemical measurements was provided by the Science of Precision Multifunctional Nanostructures for Electrical Energy Storage (NEES), an Energy Frontier Research Center funded by the U.S. DOE, Office of Science, Office of Basic Energy Sciences, under award DESC0001160 (B.S.D.). J.B.C. acknowledges support from The Clean Green IGERT (NSF DGE-0903720).

■ REFERENCES

- (1) Shen, C.; Shan, P.; Gao, T. A Comprehensive Overview of Hybrid Electric Vehicles. *Int. J. Veh. Technol.* **2011**, *2011*, 1–7.
- (2) Chan, C. C. The State of the Art of Electric, Hybrid, and Fuel Cell Vehicles. *Proc. IEEE* **2007**, *95*, 704–718.
- (3) Ozawa, K. Lithium-Ion Rechargeable Batteries with LiCoO₂ and Carbon Electrodes: The LiCoO₂/C System. *Solid State Ionics* **1994**, *69*, 212–221.
- (4) Scrosati, B. Lithium Rocking Chair Batteries: An Old Concept? *J. Electrochem. Soc.* **1992**, *139*, 2776–2781.
- (5) Guyomard, D.; Tarascon, J. Rocking-Chair or Lithium-Ion Rechargeable Lithium Batteries. *Adv. Mater.* **1994**, *6*, 408–412.
- (6) Endo, M.; Kim, C.; Nishimura, K.; Fujino, T.; Miyashita, K. Recent Development of Carbon Materials for Li Ion Batteries. *Carbon* **2000**, *38*, 183–197.
- (7) Nitta, N.; Yushin, G. High-Capacity Anode Materials for Lithium-Ion Batteries: Choice of Elements and Structures for Active Particles. *Part. Part. Syst. Charact.* **2014**, *31*, 317–336.
- (8) Zhang, W. J. A Review of the Electrochemical Performance of Alloy Anodes for Lithium-Ion Batteries. *J. Power Sources* **2011**, *196*, 13–24.
- (9) McDowell, M. T.; Lee, S. W.; Nix, W. D.; Cui, Y. 25th Anniversary Article: Understanding the Lithiation of Silicon and Other Alloying Anodes for Lithium-Ion Batteries. *Adv. Mater.* **2013**, *25*, 4966–4985.
- (10) Beaulieu, L. Y.; Eberman, K. W.; Turner, R. L.; Krause, L. J.; Dahn, J. R. Colossal Reversible Volume Changes in Lithium Alloys. *Electrochem. Solid-State Lett.* **2001**, *4*, A137–A140.
- (11) Becker, C. R.; Strawhecker, K. E.; McAllister, Q. P.; Lundgren, C. A. In Situ Atomic Force Microscopy of Lithiation and Delithiation of Silicon Nanostructures for Lithium Ion Batteries. *ACS Nano* **2013**, *7*, 9173–9182.
- (12) Beaulieu, L. Y.; Hatchard, T. D.; Bonakdarpour, A.; Fleischauer, M. D.; Dahn, J. R. Reaction of Li with Alloy Thin Films Studied by In Situ AFM. *J. Electrochem. Soc.* **2003**, *150*, A1457–A1464.
- (13) Liu, X. H.; Zheng, H.; Zhong, L.; Huang, S.; Karki, K.; Zhang, L. Q.; Liu, Y.; Kushima, A.; Liang, W. T.; Wang, J. W.; Cho, J.-H.; Epstein, E.; Dayeh, S. A.; Picraux, S. T.; Zhu, T.; Li, J.; Sullivan, J. P.; Cumings, J.; Wang, C.; Mao, S. X.; Ye, Z. Z.; Zhang, S.; Huang, J. Y. Anisotropic Swelling and Fracture of Silicon Nanowires during Lithiation. *Nano Lett.* **2011**, *11*, 3312–3318.
- (14) Chen, S.; Bao, P.; Huang, X.; Sun, B.; Wang, G. Hierarchical 3D Mesoporous Silicon@graphene Nanoarchitectures for Lithium Ion Batteries with Superior Performance. *Nano Res.* **2014**, *7*, 85–94.
- (15) Hwa, Y.; Kim, W.-S.; Yu, B.-C.; Kim, J.-H.; Hong, S.-H.; Sohn, H.-J. Facile Synthesis of Si Nanoparticles Using Magnesium Silicide Reduction and Its Carbon Composite as a High-Performance Anode for Li Ion Batteries. *J. Power Sources* **2014**, *252*, 144–149.
- (16) Li, J.; Dudney, N. J.; Xiao, X.; Cheng, Y.-T.; Liang, C.; Verbrugge, M. W. Asymmetric Rate Behavior of Si Anodes for Lithium-Ion Batteries: Ultrafast De-Lithiation versus Sluggish Lithiation at High Current Densities. *Adv. Energy Mater.* **2015**, *5*, 1401627.
- (17) Ge, M.; Lu, Y.; Ercius, P.; Rong, J.; Fang, X.; Mecklenburg, M.; Zhou, C. Large-Scale Fabrication, 3D Tomography, and Lithium-Ion Battery Application of Porous Silicon. *Nano Lett.* **2014**, *14*, 261–268.
- (18) Kim, H.; Seo, M.; Park, M.-H.; Cho, J. A Critical Size of Silicon Nano-Anodes for Lithium Rechargeable Batteries. *Angew. Chem., Int. Ed.* **2010**, *49*, 2146–2149.
- (19) Tesfaye, A. T.; Gonzalez, R.; Coffey, J. L.; Djenizian, T. Porous Silicon Nanotube Arrays as Anode Material for Li-Ion Batteries. *ACS Appl. Mater. Interfaces* **2015**, *7*, 20495–20498.
- (20) Wada, T.; Yamada, J.; Kato, H. Preparation of Three-Dimensional Nanoporous Si Using Dealloying by Metallic Melt and Application as a Lithium-Ion Rechargeable Battery Negative Electrode. *J. Power Sources* **2016**, *306*, 8–16.
- (21) Wang, B.; Li, X.; Qiu, T.; Luo, B.; Ning, J.; Li, J.; Zhang, X.; Liang, M.; Zhi, L. High Volumetric Capacity Silicon-Based Lithium Battery Anodes by Nanoscale System Engineering. *Nano Lett.* **2013**, *13*, 5578–5584.
- (22) Yun, Q.; Qin, X.; Lv, W.; He, Y. B.; Li, B.; Kang, F.; Yang, Q. H. Concrete” Inspired Construction of a Silicon/Carbon Hybrid Electrode for High Performance Lithium Ion Battery. *Carbon* **2015**, *93*, 59–67.
- (23) Liu, J.; Kopold, P.; van Aken, P. A.; Maier, J.; Yu, Y. Energy Storage Materials from Nature through Nanotechnology: A Sustainable Route from Reed Plants to a Silicon Anode for Lithium-Ion Batteries. *Angew. Chem.* **2015**, *127*, 9768–9772.
- (24) Yu, W.; Liu, C.; Hou, P.; Zhang, L.; Shan, X.; Li, F.; Cheng, H. Lithiation of Silicon Nanoparticles Con Fi Ned in Carbon Nanotubes. *ACS Nano* **2015**, *9*, 5063–5071.
- (25) Xiao, X.; Zhou, W.; Kim, Y.; Ryu, I.; Gu, M.; Wang, C.; Liu, G.; Liu, Z.; Gao, H. Regulated Breathing Effect of Silicon Negative Electrode for Dramatically Enhanced Performance of Li-Ion Battery. *Adv. Funct. Mater.* **2015**, *25*, 1426–1433.
- (26) Zhang, H.; Braun, P. V. Three-Dimensional Metal Scaffold Supported Bicontinuous Silicon Battery Anodes. *Nano Lett.* **2012**, *12*, 2778–2783.
- (27) Peled, E.; Patolsky, F.; Golodnitsky, D.; Freedman, K.; Davidi, G.; Schneier, D. Tissue-like Silicon Nanowires-Based Three-Dimensional Anodes for High-Capacity Lithium Ion Batteries. *Nano Lett.* **2015**, *15*, 3907–3916.
- (28) Wada, T.; Ichitsubo, T.; Yubuta, K.; Segawa, H.; Yoshida, H.; Kato, H. Bulk-Nanoporous-Silicon Negative Electrode with Extremely High Cyclability for Lithium-Ion Batteries Prepared Using a Top-down Process. *Nano Lett.* **2014**, *14*, 4505–4510.

- (29) Zhou, M.; Li, X.; Wang, B.; Zhang, Y.; Ning, J.; Xiao, Z.; Zhang, X.; Chang, Y.; Zhi, L. High-Performance Silicon Battery Anodes Enabled by Engineering Graphene Assemblies. *Nano Lett.* **2015**, *15*, 6222–6228.
- (30) Son, Y.; Son, Y.; Choi, M.; Ko, M.; Chae, S.; Park, N.; Cho, J. Hollow Silicon Nanostructures via the Kirkendall Effect. *Nano Lett.* **2015**, *15*, 6914–6918.
- (31) Wang, W.; Favors, Z.; Ionescu, R.; Ye, R.; Bay, H. H.; Ozkan, M.; Ozkan, C. S. Monodisperse Porous Silicon Spheres as Anode Materials for Lithium Ion Batteries. *Sci. Rep.* **2015**, *5*, 1–6.
- (32) Liu, N.; Lu, Z.; Zhao, J.; McDowell, M. T.; Lee, H.-W.; Zhao, W.; Cui, Y. A Pomegranate-Inspired Nanoscale Design for Large-Volume-Change Lithium Battery Anodes. *Nat. Nanotechnol.* **2014**, *9*, 187–192.
- (33) Lin, D.; Lu, Z.; Hsu, P.-C.; Lee, H. R.; Liu, N.; Zhao, J.; Wang, H.; Liu, C.; Cui, Y. A High Tap Density Secondary Silicon Particle Anode Fabricated by Scalable Mechanical Pressing for Lithium-Ion Batteries. *Energy Environ. Sci.* **2015**, *8*, 2371–2376.
- (34) Chan, C. K.; Peng, H.; Liu, G.; McIlwrath, K.; Zhang, X. F.; Huggins, R. A.; Cui, Y. High-Performance Lithium Battery Anodes Using Silicon Nanowires. *Nat. Nanotechnol.* **2008**, *3*, 31–35.
- (35) Cui, L.-F.; Ruffo, R.; Chan, C. K.; Peng, H.; Cui, Y. Crystalline-Amorphous Core–Shell Silicon Nanowires for High Capacity and High Current Battery Electrodes. *Nano Lett.* **2009**, *9*, 491–495.
- (36) Cui, L.-F.; Yang, Y.; Hsu, C.-M.; Cui, Y. Carbon - Silicon Core - Shell Nanowires as High Capacity Electrode for Lithium Ion Batteries. *Nano Lett.* **2009**, *9*, 3370–3372.
- (37) Chan, C. K.; Patel, R. N.; O’Connell, M. J.; Korgel, B. A.; Cui, Y. Solution-Grown Silicon Nanowires for Lithium-Ion Battery Anodes. *ACS Nano* **2010**, *4*, 1443–1450.
- (38) Song, T.; Xia, J.; Lee, J.-H.; Lee, D. H.; Kwon, M.-S.; Choi, J.-M.; Wu, J.; Doo, S. K.; Chang, H.; Park, W. I.; Zang, D. S.; Kim, H.; Huang, Y.; Hwang, K.-C.; Rogers, J. a; Paik, U. Arrays of Sealed Silicon Nanotubes as Anodes for Lithium Ion Batteries. *Nano Lett.* **2010**, *10*, 1710–1716.
- (39) Yao, Y.; McDowell, M. T.; Ryu, I.; Wu, H.; Liu, N.; Hu, L.; Nix, W. D.; Cui, Y. Interconnected Silicon Hollow Nanospheres for Lithium-Ion Battery Anodes with Long Cycle Life. *Nano Lett.* **2011**, *11*, 2949–2954.
- (40) Nishio, K.; Tagawa, S.; Fukushima, T.; Masuda, H. Highly Ordered Nanoporous Si for Negative Electrode of Rechargeable Lithium-Ion Battery. *Electrochem. Solid-State Lett.* **2012**, *15*, A41–A44.
- (41) Ge, M.; Fang, X.; Rong, J.; Zhou, C. Review of Porous Silicon Preparation and Its Application for Lithium-Ion Battery Anodes. *Nanotechnology* **2013**, *24*, 422001.
- (42) Kim, H.; Han, B.; Choo, J.; Cho, J. Three-Dimensional Porous Silicon Particles for Use in High-Performance Lithium Secondary Batteries. *Angew. Chem., Int. Ed.* **2008**, *47*, 10151–10154.
- (43) Yu, Y.; Gu, L.; Zhu, C.; Tsukimoto, S.; van Aken, P. A.; Maier, J. Reversible Storage of Lithium in Silver-Coated Three-Dimensional Macroporous Silicon. *Adv. Mater.* **2010**, *22*, 2247–2250.
- (44) Jia, H.; Gao, P.; Yang, J.; Wang, J.; Nuli, Y.; Yang, Z. Novel Three-Dimensional Mesoporous Silicon for High Power Lithium-Ion Battery Anode Material. *Adv. Energy Mater.* **2011**, *1*, 1036–1039.
- (45) Chen, W.; Fan, Z.; Dhanabalan, A.; Chen, C.; Wang, C. Mesoporous Silicon Anodes Prepared by Magnesiothermic Reduction for Lithium Ion Batteries. *J. Electrochem. Soc.* **2011**, *158*, A1055–A1059.
- (46) Jiang, Z.; Li, C.; Hao, S.; Zhu, K.; Zhang, P. An Easy Way for Preparing High Performance Porous Silicon Powder by Acid Etching Al-Si Alloy Powder for Lithium Ion Battery. *Electrochim. Acta* **2014**, *115*, 393–398.
- (47) Chun, M.-J.; Park, H.; Park, S.; Choi, N.-S. Bicontinuous Structured Silicon Anode Exhibiting Stable Cycling Performance at Elevated Temperature. *RSC Adv.* **2013**, *3*, 21320–21325.
- (48) Lv, Q.; Liu, Y.; Ma, T.; Zhu, W.; Qiu, X. Hollow Structured Silicon Anodes with Stabilized Solid Electrolyte Interphase Film for Lithium-Ion Batteries. *ACS Appl. Mater. Interfaces* **2015**, *7*, 23501–23506.
- (49) Zhou, Y.; Jiang, X.; Chen, L.; Yue, J.; Xu, H.; Yang, J.; Qian, Y. Novel Mesoporous Silicon Nanorod as an Anode Material for Lithium Ion Batteries. *Electrochim. Acta* **2014**, *127*, 252–258.
- (50) Cheng, H.; Xiao, R.; Bian, H.; Li, Z.; Zhan, Y.; Tsang, C. K.; Chung, C. Y.; Lu, Z.; Li, Y. Y. Periodic Porous Silicon Thin Films with Interconnected Channels as Durable Anode Materials for Lithium Ion Batteries. *Mater. Chem. Phys.* **2014**, *144*, 25–30.
- (51) Kim, Y. K.; Moon, J. W.; Lee, J. G.; Baek, Y. K.; Hong, S. H. Porous Carbon-Coated Silica Macroparticles as Anode Materials for Lithium Ion Batteries: Effect of Boric Acid. *J. Power Sources* **2014**, *272*, 689–695.
- (52) Cho, Y.-S.; Kim, Y.-K.; Kim, S.-H.; Lim, D. C.; Lee, J.-G.; Baek, Y.-K.; Yi, G.-R. Spherical Meso-Macroporous Silica Particles by Emulsion-Assisted Dual-Templating. *Mater. Express* **2014**, *4*, 91–104.
- (53) Kasavajjula, U.; Wang, C.; Appleby, A. J. Nano- and Bulk-Silicon-Based Insertion Anodes for Lithium-Ion Secondary Cells. *J. Power Sources* **2007**, *163*, 1003–1039.
- (54) Ma, D.; Cao, Z.; Hu, A. Si-Based Anode Materials for Li-Ion Batteries: A Mini Review. *Nano-Micro Lett.* **2014**, *6*, 347–358.
- (55) Su, X.; Wu, Q.; Li, J.; Xiao, X.; Lott, A.; Lu, W.; Sheldon, B. W.; Wu, J. Silicon-Based Nanomaterials for Lithium-Ion Batteries. *Adv. Energy Mater.* **2014**, *4*, 1300882.
- (56) Luo, F.; Liu, B.; Zheng, J.; Chu, G.; Zhong, K.; Li, H.; Huang, X.; Chen, L. Review—Nano-Silicon/Carbon Composite Anode Materials Towards Practical Application for Next Generation Li-Ion Batteries. *J. Electrochem. Soc.* **2015**, *162*, A2509–A2528.
- (57) Roy, P.; Srivastava, S. K. Nanostructured Anode Materials for Lithium Ion Batteries. *J. Mater. Chem. A* **2015**, *3*, 2454–2484.
- (58) Bley, R. A.; Kauzlarich, S. M.; Davis, J. E.; Lee, H. W. H. Characterization of Silicon Nanoparticles Prepared from Porous Silicon. *Chem. Mater.* **1996**, *8*, 1881–1888.
- (59) Shin, Y.; Wang, C.; Exarhos, G. J. Synthesis of SiC Ceramics by the Carbothermal Reduction of Mineralized Wood with Silica. *Adv. Mater.* **2005**, *17*, 73–77.
- (60) Bao, Z.; Weatherspoon, M. R.; Shian, S.; Cai, Y.; Graham, P. D.; Allan, S. M.; Ahmad, G.; Dickerson, M. B.; Church, B. C.; Kang, Z.; Abernathy, H. W., III; Summers, C. J.; Liu, M.; Sandhage, K. H. Chemical Reduction of Three-Dimensional Silica Micro-Assemblies into Microporous Silicon Replicas. *Nature* **2007**, *446*, 172–175.
- (61) Liu, N.; Huo, K.; McDowell, M. T.; Zhao, J.; Cui, Y. Rice Husks as a Sustainable Source of Nanostructured Silicon for High Performance Li-Ion Battery Anodes. *Sci. Rep.* **2013**, *3*, 1919.
- (62) Yanagisawa, T.; Shimizu, T.; Kuroda, K.; Kato, C. The Preparation of Alkyltrimethylammonium-Kanemite Complexes and Their Conversion to Microporous Materials. *Bull. Chem. Soc. Jpn.* **1990**, *63*, 988–992.
- (63) Yang, P.; Zhao, D.; Margolese, D. I.; Chmelka, B. F.; Stucky, G. D. Block Copolymer Templating Syntheses of Mesoporous Metal Oxides with Large Ordering Lengths and Semicrystalline Framework. *Chem. Mater.* **1999**, *11*, 2813–2826.
- (64) Orilall, M. C.; Wiesner, U. Block Copolymer Based Composition and Morphology Control in Nanostructured Hybrid Materials for Energy Conversion and Storage: Solar Cells, Batteries, and Fuel Cells. *Chem. Soc. Rev.* **2011**, *40*, 520–535.
- (65) Möller, K.; Kobler, J.; Bein, T. Colloidal Suspensions of Nanometer-Sized Mesoporous Silica. *Adv. Funct. Mater.* **2007**, *17*, 605–612.
- (66) Jin, J.; Huang, S.-Z.; Liu, J.; Li, Y.; Chen, D.-S.; Wang, H.-E.; Yu, Y.; Chen, L.-H.; Su, B.-L. Design of New Anode Materials Based on Hierarchical, Three Dimensional Ordered Macro-Mesoporous TiO₂ for High Performance Lithium Ion Batteries. *J. Mater. Chem. A* **2014**, *2*, 9699–9708.
- (67) Feckl, J. M.; Fominykh, K.; Döblinger, M.; Fattakhova-Rohlfing, D.; Bein, T. Nanoscale Porous Framework of Lithium Titanate for Ultrafast Lithium Insertion. *Angew. Chem., Int. Ed.* **2012**, *51*, 7459–7463.
- (68) Simon, P. F. W.; Ulrich, R.; Spiess, H. W.; Wiesner, U. Block Copolymer - Ceramic Hybrid Materials from Organically Modified Ceramic Precursors. *Chem. Mater.* **2001**, *13*, 3464–3486.

- (69) Brezesinski, K.; Wang, J.; Haetge, J.; Reitz, C.; Steinmueller, S. O.; Tolbert, S. H.; Smarsly, B. M.; Dunn, B.; Brezesinski, T. Pseudocapacitive Contributions to Charge Storage in Highly Ordered Mesoporous Group v Transition Metal Oxides with Iso-Oriented Layered Nanocrystalline Domains. *J. Am. Chem. Soc.* **2010**, *132*, 6982–6990.
- (70) Brezesinski, T.; Wang, J.; Tolbert, S. H.; Dunn, B. Ordered Mesoporous Alpha-MoO₃ with Iso-Oriented Nanocrystalline Walls for Thin-Film Pseudocapacitors. *Nat. Mater.* **2010**, *9*, 146–151.
- (71) Kondo, J. N.; Domen, K. Crystallization of Mesoporous Metal Oxides. *Chem. Mater.* **2008**, *20*, 835–847.
- (72) Rauda, I. E.; Buonsanti, R.; Saldarriaga-Lopez, L. C.; Benjauthrit, K.; Schelhas, L. T.; Stefik, M.; Augustyn, V.; Ko, J.; Dunn, B.; Wiesner, U.; Milliron, D. J.; Tolbert, S. H. General Method for the Synthesis of Hierarchical Nanocrystal-Based Mesoporous Materials. *ACS Nano* **2012**, *6*, 6386–6399.
- (73) Deng, Y.; Yu, T.; Wan, Y.; Shi, Y.; Meng, Y.; Gu, D.; Zhang, L.; Huang, Y.; Liu, C.; Wu, X.; Zhao, D. Ordered Mesoporous Silicas and Carbons with Large Accessible Pores Templated from Amphiphilic Diblock Copolymer Poly(ethylene Oxide)-B-Polystyrene. *J. Am. Chem. Soc.* **2007**, *129*, 1690–1697.
- (74) Richman, E. K.; Kang, C. B.; Brezesinski, T.; Tolbert, S. H. Ordered Mesoporous Silicon through Magnesium Reduction of Polymer Templated Silica Thin Films. *Nano Lett.* **2008**, *8*, 3075–3079.
- (75) Deng, Y.; Wei, J.; Sun, Z.; Zhao, D. Large-Pore Ordered Mesoporous Materials Templated from Non-Pluronic Amphiphilic Block Copolymers. *Chem. Soc. Rev.* **2013**, *42*, 4054–4070.
- (76) Wei, J.; Wang, H.; Deng, Y.; Sun, Z.; Shi, L.; Tu, B.; Luqman, M.; Zhao, D. To Three-Dimensional Ordered Mesoporous Silica with Ultralarge Accessible Mesopores. *J. Am. Chem. Soc.* **2011**, *133*, 20369–20377.
- (77) Brezesinski, T.; Fischer, A.; Iimura, K. I.; Sanchez, C.; Grosso, D.; Antonietti, M.; Smarsly, B. M. Generation of Self-Assembled 3D Mesostructured SnO₂ Thin Films with Highly Crystalline Frameworks. *Adv. Funct. Mater.* **2006**, *16*, 1433–1440.
- (78) Smarsly, B.; Grosso, D.; Brezesinski, T.; Pinna, N.; Boissiere, C.; Antonietti, M.; Sanchez, C. Highly Crystalline Cubic Mesoporous TiO₂ with 10-Nm Pore Diameter Made with a New Block Copolymer Template. *Chem. Mater.* **2004**, *16*, 2948–2952.
- (79) Brezesinski, T.; Fattakhova Rohlfing, D.; Sallard, S.; Antonietti, M.; Smarsly, B. M. Highly Crystalline WO₃ Thin Films with ordered 3D Mesoporosity and Improved Electrochromic Performance. *Small* **2006**, *2*, 1203–1211.
- (80) Groenewolt, M.; Antonietti, M.; Polarz, S. Mixed Micellar Phases of Nonmiscible Surfactants: Mesoporous Silica with Bimodal Pore Size Distribution via the Nanocasting Process. *Langmuir* **2004**, *20*, 7811–7819.
- (81) Brezesinski, T.; Antonietti, M.; Groenewolt, M.; Pinna, N.; Smarsly, B. The Generation of Mesostructured Crystalline CeO₂, ZrO₂ and CeO₂-ZrO₂ Films Using Evaporation-Induced Self-Assembly. *New J. Chem.* **2005**, *29*, 237–242.
- (82) Deshpande, A. S.; Pinna, N.; Smarsly, B.; Antonietti, M.; Niederberger, M. Controlled Assembly of Preformed Ceria Nanocrystals into Highly Ordered 3D Nanostructures. *Small* **2005**, *1*, 313–316.
- (83) Brezesinski, T.; Smarsly, B.; Iimura, K. I.; Grosso, D.; Boissiere, C.; Amenitsch, H.; Antonietti, M.; Sanchez, C. Self-Assembly and Crystallization Behavior of Mesoporous, Crystalline HfO₂ Thin Films: A Model System for the Generation of Mesostructured Transition-Metal Oxides. *Small* **2005**, *1*, 889–898.
- (84) Grosso, D.; Boissiere, C.; Smarsly, B.; Brezesinski, T.; Pinna, N.; Albouy, P. A.; Amenitsch, H.; Antonietti, M.; Sanchez, C. Periodically Ordered Nanoscale Islands and Mesoporous Films Composed of Nanocrystalline Multimetallic Oxides. *Nat. Mater.* **2004**, *3*, 787–792.
- (85) Thomas, A.; Schlaad, H.; Smarsly, B.; Antonietti, M. Replication of Lyotropic Block Copolymer Mesophases into Porous Silica by Nanocasting: Learning about Finer Details of Polymer Self-Assembly. *Langmuir* **2003**, *19*, 4455–4459.
- (86) Bloch, E.; Llewellyn, P. L.; Phan, T.; Bertin, D.; Hornebecq, V. On Defining a Simple Empirical Relationship to Predict the Pore Size of Mesoporous Silicas Prepared from PEO-B-PS Diblock Copolymers. *Chem. Mater.* **2009**, *21*, 48–55.
- (87) Jung, D. S.; Ryou, M.-H.; Sung, Y. J.; Park, S. B.; Choi, J. W. Recycling Rice Husks for High-Capacity Lithium Battery Anodes. *Proc. Natl. Acad. Sci. U. S. A.* **2013**, *110*, 12229–12234.
- (88) Lestriez, B.; Desaeve, S.; Danet, J.; Moreau, P.; Plée, D.; Guyomard, D. Hierarchical and Resilient Conductive Network of Bridged Carbon Nanotubes and Nanofibers for High-Energy Si Negative Electrodes. *Electrochem. Solid-State Lett.* **2009**, *12*, A76–A80.
- (89) Lestriez, B. Functions of Polymers in Composite Electrodes of Lithium Ion Batteries. *C. R. Chim.* **2010**, *13*, 1341–1350.
- (90) Hench, L. L.; West, J. K. The Sol-Gel Process. *Chem. Rev.* **1990**, *90*, 33–72.
- (91) Barrett, E. P.; Joyner, L. G.; Halenda, P. P. The Determination of Pore Volume and Area Distributions in Porous Substances. *J. Am. Chem. Soc.* **1951**, *73*, 373–380.
- (92) Nguyen, T. P.; Lefrant, S. Study of SiO₂ Thin Films and SiQ₂ Metal Interfaces. *J. Phys.: Condens. Matter* **1989**, *1*, 5197–5204.
- (93) Luo, W.; Wang, X.; Meyers, C.; Wannemacher, N.; Sirisaksoontorn, W.; Lerner, M. W.; Ji, X. Efficient Fabrication of Nanoporous Si and Si/Ge Enabled by a Heat Scavenger in Magnesiothermic Reactions. *Sci. Rep.* **2013**, *3*, 2222.
- (94) Li, J.; Dahn, J. R. An In Situ X-Ray Diffraction Study of the Reaction of Li with Crystalline Si. *J. Electrochem. Soc.* **2007**, *154*, A156–A161.
- (95) Choi, N. S.; Yew, K. H.; Lee, K. Y.; Sung, M.; Kim, H.; Kim, S. S. Effect of Fluoroethylene Carbonate Additive on Interfacial Properties of Silicon Thin-Film Electrode. *J. Power Sources* **2006**, *161*, 1254–1259.
- (96) Lin, Y.-M.; Klavetter, K. C.; Abel, P. R.; Davy, N. C.; Snider, J. L.; Heller, A.; Mullins, C. B. High Performance Silicon Nanoparticle Anode in Fluoroethylene Carbonate-Based Electrolyte for Li-Ion Batteries. *Chem. Commun.* **2012**, *48*, 7268–7270.
- (97) Ning, G.; Haran, B.; Popov, B. N. Capacity Fade Study of Lithium-Ion Batteries Cycled at High Discharge Rates. *J. Power Sources* **2003**, *117*, 160–169.
- (98) Harris, S. J.; Timmons, A.; Baker, D. R.; Monroe, C. Direct in Situ Measurements of Li Transport in Li-Ion Battery Negative Electrodes. *Chem. Phys. Lett.* **2010**, *485*, 265–274.
- (99) Lu, W.; López, C. M.; Liu, N.; Vaughey, J. T.; Jansen, A.; Dees, D. W. Overcharge Effect on Morphology and Structure of Carbon Electrodes for Lithium-Ion Batteries. *J. Electrochem. Soc.* **2012**, *159*, A566–A570.